Powder Technology 405 (2022) 117557

Contents lists available at ScienceDirect

Powder Technology

journal homepage: www.journals.elsevier.com/powder-technology

Discrete Element Modeling (DEM) simulations of powder bed densification using horizontal compactors in metal additive manufacturing

Vishnu V. Ganesan [a], Amirhesam Amerinatanzi [a,b], Ankur Jain [a,*]

[a] Mechanical and Aerospace Engineering Department, University of Texas at Arlington, Arlington, TX, USA
[b] Materials Science and Engineering Department, University of Texas at Arlington, Arlington, TX, USA

HIGHLIGHTS

- Presents Discrete Element Modeling (DEM) based simulations of powder spreading process in metal additive manufacturing.
- Discusses the role of dynamic bed walls for improved densification of the spread powder layer.
- Results are in good agreement with past work by Wang, et al. (2021).
- Results predict significant improvement in powder bed void fraction and stresses on underneath layer.
- Results may help in design and optimization of powder-based additive manufacturing processes.

GRAPHICAL ABSTRACT

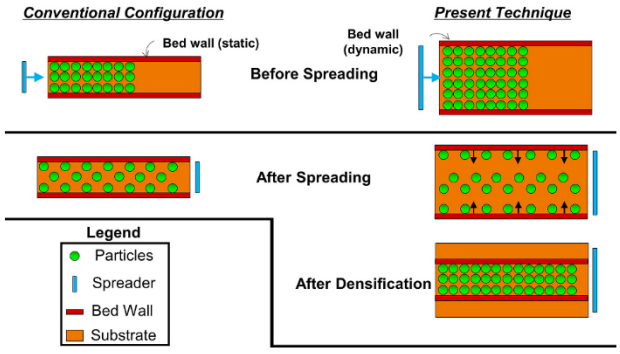

ARTICLE INFO

Keywords:
Additive manufacturing
Powder Bed Fusion (PBF)
Discrete Element Method (DEM)
Horizontal compaction

ABSTRACT

Efficient packing of the powder bed plays a key role in ensuring high quality of parts printed with Powder Bed Fusion (PBF) based additive manufacturing technologies. This paper presents simulations and analysis of a new technique based on horizontal compactors for improved densification of the spread powder layer. Discrete Element Modeling (DEM) based simulation of this technique shows much improved bed densification and force reduction on the layer underneath, thereby contributing to improved part quality. Results are found to be in excellent agreement with past work. Simulations predict the void fraction distribution as a function of various process parameters. Simulations are carried out to understand the effect of number of particles on stresses acting on the previously printed layer. The technique discussed here is a general one, and may also help analyze other powder-based additive manufacturing processes such as selective laser sintering and binder jetting.

1. Introduction

Additive Manufacturing (AM) is a class of advanced manufacturing techniques, in which, the part of interest is formed in a selective, layer-by-layer fashion [1]. A number of different material types, such as metals, polymers and composites have been manufactured using AM techniques [2,3]. Compared to traditional, subtractive manufacturing techniques, AM enables the printing of parts with complex geometries and organic structures. AM also facilitates topological optimization in a significantly expanded design space [4]. However, due to the discrete

* Corresponding author at: 500 W First St, Rm 211, Arlington, TX 76019, USA.
E-mail address: jaina@uta.edu (A. Jain).

https://doi.org/10.1016/j.powtec.2022.117557
Received 25 March 2022; Received in revised form 5 May 2022; Accepted 22 May 2022
Available online 26 May 2022

nature of AM, 3D printed parts often suffer from deteriorated performance compared to base materials [5]. Anisotropicity in thermal/mechanical properties and geometrical distortion are also often serious concerns in additive manufacturing [6,7].

Within the context of metal-based AM, Powder Bed Fusion (PBF) is a class of techniques, in which an energy source is used to selectively melt and bind powder particles spread on a platform bed to form the cross-section of interest [3,8,9]. PBF techniques are usually classified based on the energy source, such as laser PBF and electron beam PBF [3,9], each offering its own advantages. PBF mainly comprises three steps – powder recoating, energy input, and finally, coalescence and cooling [8]. Powder recoating is accomplished by means of a spreader, which moves across the substrate to deposit the powder particles and generates a powder layer of the intended thickness [10]. All three processes contribute towards determining the nature of melt pool geometry obtained, which, in turn, determines the quality of the build part [11]. However, controlling the quality of powder layer during its formation is extremely difficult, as it is mainly governed by spreader geometry, speed, particle size distribution, and layer thickness [12,13].

Thermally-driven techniques such as pre-sintering of laser powders using an in situ auxiliary heat source or post-process heat treatments are commonly used to improve part quality in PBF [14–17]. Such active techniques are often energy intensive and may cause significant distortion in part geometry [18]. In contrast with such heat-driven techniques, improving the density of powder bed is also a potential mechanism to reduce porosity in the built part without the adverse effects associated with heat-driven techniques. In this context, the chamber walls may play a key role in corralling the powder particles. The chamber walls, which are primarily used for containment interact with the powder particles by imposing friction during spreading [19]. While chamber walls have traditionally been assumed to be static, there may be some benefits of considering a moving, dynamic wall which allows for compaction of the powder bed.

Due to the considerable cost and complexity of experiments, simulations of the powder spreading process may play an important role in understanding and optimizing process parameters in order to improve part quality in PBF. The problem of spreading and densifying a powder bed in PBF is a multiscale problem due to the large variation in length scales present, ranging from the microscopic size of a single particle to the macroscopic printed part [20]. This makes the problem difficult to simulate using standard tools, such as the Finite Element Method (FEM). The challenge of simulating a large number of particles present has also been recognized in the literature and various simulation techniques have been explored for this problem [21].

A commonly used technique for simulating the spreading of a powder bed is the Discrete Element Method (DEM), which has been used extensively to capture and characterize the quality of the powder layer formed [22–24]. Powder layer spreading has been characterized using DEM simulations, in which, particle segregation has been captured using particle size distribution and the void fraction has been calculated using the co-ordination number of the formed powder layer [22,23]. Characteristics of the final state of powder bed for different spreader speeds has been presented [25,26]. These papers also present analysis of the effect of spreader speed on particle segregation. Improvement in the quality of the powder layer through spreader geometry enhancement has been reported through DEM analysis. For example, a spreader with a super-elliptic edge geometry has been shown to result in denser packing close to that of a roller [27]. Void fraction and surface roughness were used to determine the bed quality in this work. A related paper showed that packing density increases with increase in layer thickness, but at the cost of reduced geometrical accuracy of the printed part [28]. The effect of particle size distribution and shape on the powder bed density has been studied [29]. Smaller particles were shown to increase packing density, but at the cost of reduced flowability and spreadability due to Van der Waals forces. Mono-sized particles were found to produce greater porosity than multi-sized particles because particles of different sizes can efficiently occupy the gaps generated during spreading [30]. Surface energy of the powder particles and its effect on adhesion between the sintered molten part and the spread powder layer has been extensively studied [31].

Forces exerted on the underneath layer during the spreading process have been widely characterized in such DEM simulations. Deformation due to shearing of powder particles weas analyzed for different speeds of spreader in [32]. Distortion of green part due to different dimensions of spreader blade was studied and experimentally validated [33]. Although these papers characterized the effect of spreading on the part underneath, a proper force analysis was not performed. A study of downwards forces during the spreading process for various spreader geometry has been presented [34]. Force chain analysis was used to explain the higher force transmission from the spreader to the substrate via the powder particles. In another work, DEM was used to compute the forces acting on the spreader for non-spherical particles during the spreading process [35]. DEM-based analysis of the spreading process has been used for laser sintering as well [36,37]. Some work on FEM-based analysis of powder bed spreading has also be reported [38], although such literature is very limited compared to DEM-based analysis.

During the spreading process, powder particles form force chains that are responsible for determining the forces acting on the underneath layer. A force chain is a group of in-contact granular material that effectively transmit external forces from one point to another [39]. The layer underneath is susceptible to deformation and loss of build accuracy, and, therefore, the magnitude of force chains within the powder layer must be as low as possible [34]. Spreading the particles over a large surface area so that the particles are spread apart would be ideal, as the number of stress-transmitting force chains is directly proportional to the bulk density of the powder particles [40]. However, spreading loosely packed powder might not result in a sufficiently dense powder bed to be sintered accurately. In contrast with the present state-of-the-art comprising static bed walls, this tradeoff may be effectively managed by using horizontal compactors that may move in order to further densify the powder bed after loose spreading. A DEM simulation of die compaction was carried out in order to capture the compact response in [41]. Despite the sizable literature on powder bed densification strategies, such as the papers summarized above, there is a lack of investigation of horizontal compactors and the impact on powder bed densification.

The present work, for the first time, investigates the impact of horizontal compactors to densify the loosely packed powder bed after spreading. This densification by the motion of horizontal compactors occurs after spreading and before laser melting. Fig. 1 illustrates this concept by showing geometrical schematics of the conventional configuration and the one proposed here with horizontal compactors. A DEM based simulation using LIGGGHTS software is developed for understanding how horizontal compactors decrease the inter-particle force and stress acting on the underneath layer. Using void fraction within the powder bed as an indirect measure of the packing density, the impact of horizontal compactors on bed densification is presented. Results from this work may help develop a better understanding of powder bed densification, potentially leading to improved quality of parts printed using PBF.

2. Simulation setup

This section outlines the procedure followed for simulations presented in this work. Two sets of simulations are carried out. In the first set, the conventional configuration with static walls shown in Fig. 1(a) is simulated, and in the second set, a configuration with horizontal compactors shown in Fig. 1(b) is simulated. The DEM simulation framework for both the sets is first discussed, followed by specific details of CFD-DEM coupling.

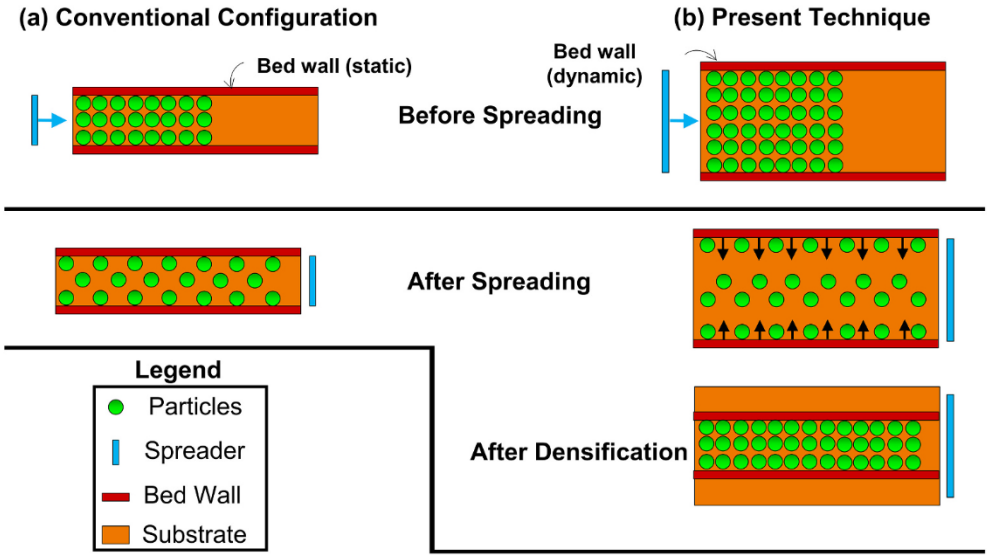

Fig. 1. Schematic of a powder bed configuration showing top views of the powder bed before and after spreading. Both conventional configuration and the present technique are shown for illustration and comparison.

2.1. Discrete element model for conventional powder bed configuration

The system under consideration here comprises the platform bed, a large number of powder particles of relatively small diameter with a given size distribution as well as the spreader and wall. Numerical simulations of the spreading and densification of the powder bed are carried out using DEM implemented in LIGGGHTS software [42]. The motion of the powder particles is computed by numerical integration of the acceleration of each particle obtained from the net force acting on each particle, in accordance with Newton's second law of motion. This helps pinpoint the displacement and therefore the location of each particle at every timestep. Despite not solving the full set of governing equations, DEM is a reasonable approximation and enables force chain analysis [43], which is particularly important for the present problem.

The process of powder bed generation consists of loading the substrate with powder particles and then using a spreader to level out the powder to the required height. Geometrical models of the spreader and substrate are designed in SOLIDWORKS and imported into the LIGGGHTS simulation framework. The conventional configuration of the powder bed is shown schematically in Fig. 2(a). All dimensional values shown in this and subsequent Figures are in mm. The substrate is a rectangular block of size 18 mm by 0.5 mm and height 0.5 mm, consistent with past work [34]. The spreader consists of a flat vertical blade positioned at a height of 70 μm from the substrate, which denotes the layer height. A total of 35,000 powder particles with a particle size distribution that is close to normal distribution in the 5–65 μm diameter range are generated. The distribution of particles is designed to be similar to past work [34]. i.e., 10%, 25% and 90% of the particle are smaller than a diameter of 25.9 μm, 39.4 μm and 52.7 μm, respectively. The Hertz tangential model with SJKR (Simplified Johnson-Kendall-Roberts) model [44] is used to calculate the forces on each particle. The Hertz granular model calculates the frictional force between two granular particles at a given distance, while the SJKR model computes the normal force. The coefficient of friction and cohesive energy density are important parameters needed as inputs for the simulation. These and other powder parameters used in the model are listed in Table 1.

Simulations for the conventional configuration are started by randomly generating particles on the powder bed using rain drop method [45], in which, the particles fall from a certain height onto the substrate. Once the particles settle down, spreader motion in the *x*

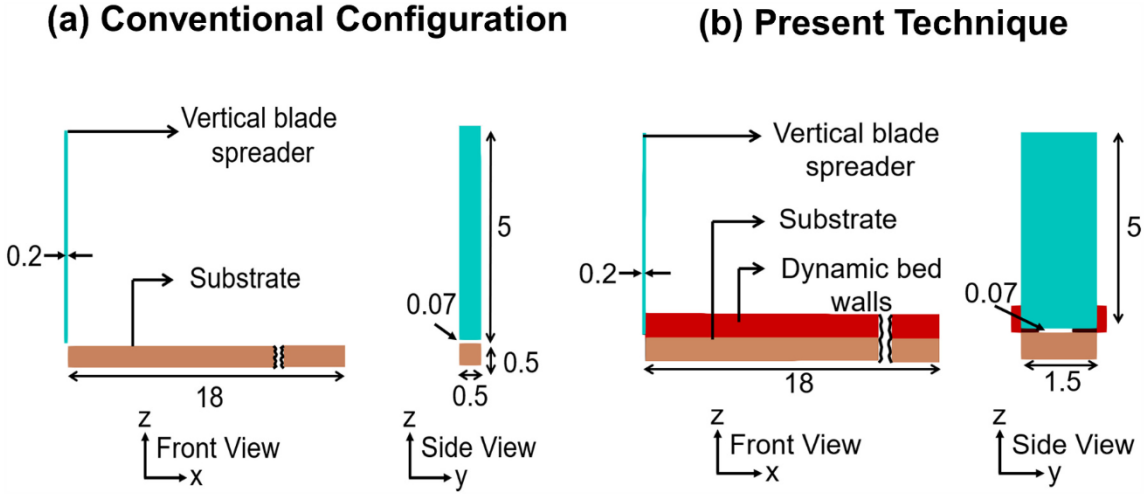

Fig. 2. Schematic of a powder bed configuration showing the vertical blade spreader used for powder spreading on a substrate. (a) and (b) show the conventional configuration and the present technique, respectively. All units in this and subsequent Figures are in mm.

Table 1
Values of various process parameters and properties used in the past work. All values are taken from [34].

Parameter	Value	Units
Sliding friction coefficient	0.3 (particle-to-particle), 0.9 (particle-to-wall)	–
Rolling friction coefficient	0.005 (particle-to-particle), 0.005 (particle-to-wall)	–
Particle diameter	5–65	μm
Particle density	8200	kg/m^3
Young's modulus of particle	1	GPa
Restitution coefficient	0.35 (particle-to-particle), 0.35 (particle-to-wall)	–
Poisson's ratio of particle	0.3	–
Spreading speed	0.05	m/s
Layer gap	70	μm
Cohesion Energy Density	1	MJ/m^3

direction at a constant speed of 0.05 m/s is implemented. Results from a typical simulation of the spreading process are shown in Fig. 3, where the powder bed configuration is depicted at three different times –the initial time ($t = 0$ s), the time at which the spreader is at halfway along the substrate ($t = 180$ s) and the time at which the spreading process is complete ($t = 360$ s). Particles of different sizes at these stages are visualized clearly in the form of zoomed-in images included in Fig. 3.

2.2. Discrete element model for present technique with horizontal compactors

In order to simulate the effect of a horizontal compactor through simulations, the spreader size is increased along the *y*-direction from 0.5 mm to 1.5 mm. Two walls of the same thickness as the vertical spreader are modeled on either side of the substrate, as shown in Fig. 2(b). The effect of densification speed and the number of particles on the stresses acting on the previously printed layer is simulated. Powder bed density and void fraction are computed using CFD-DEM coupling, as outlined in the next section.

2.3. CFD-DEM coupling of LIGGGHTS and OpenFoam

Void fraction is a key metric for understanding the quality of the powder layer deposition and densification. The void fraction may be interpreted as an indirect measure of the bulk density of the powder bed [46]. Void fraction analysis cannot be carried out directly in LIGGGHTS. As a result, OpenFoam simulation software for Computational Fluid Dynamics (CFD) [47] is used. A fluid domain containing air is designed on top of the substrate as shown in Fig. 4. This domain is then meshed with 173,000 elements and sliced along three equidistant sections X1, X2, X3, as shown. Each cell initially contains air. As the spreader moves, the powder particles begin to occupy the domain by displacing the air. As a result, each element now contains both air and powder in a certain ratio. The location of powder particles at each time step is transferred from LIGGGHTS to OpenFoam by a technique called CFD-DEM coupling [48]. The ratio of air volume to the total volume within each cell is then computed as the local void fraction, which is integrated over the entire bed to determine the overall void fraction of the entire powder layer. Please note that since the goal here is simply to calculate the void fraction, therefore, the role of OpenFoam is limited only to determining void fraction distribution based on the imported geometry. No CFD calculations are needed to be carried out for this purpose.

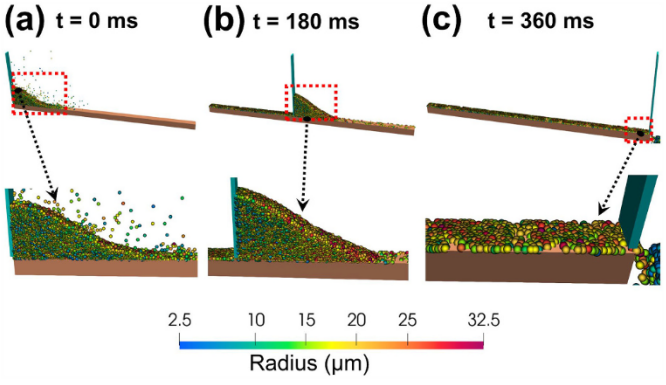

Fig. 3. Typical DEM simulation results showing powder layer formation as the blade moves along the length of the substrate with a spreading speed of 0.05 m/s at three different times: a) 0 ms, b) 180 ms, and c) 360 ms. Zoom-in images are shown for each time. Particle color corresponds to its size.

3. Results and discussion

3.1. Model validation

A comparison of the present work with a past simulation using a vertical blade model by Wang, et al. [34] is carried out first. In this past work, simulation of powder bed generation using a different spreader geometry was reported. This paper carried out a force chain analysis and computed the average forces on the previously printed layer from the particle bed along with inter-particle forces over the entire simulation time. The vertical blad geometry used in the present work is similar to the conventional configuration simulation in the past work. For comparison, all other parameters in the present simulation are chosen to match the values in the past work, as listed in Table 1. Specifically, the spreader speed is 0.05 m/s and the layer thickness is 70 μm. The cohesion energy density listed in Table 1 is calculated based on the values of Hamaker constant and cut-off distance used by Wang, et al. [34]. The coefficient of sliding friction between the particles and the substrate is assumed to be 0.9. Due to the high value of this coefficient, significant shear force is expected to be generated as the powder particles slide over the layer underneath. In addition, a normal force due to self-weight of the particles acts downwards. Based on the force balance computed during DEM simulations, the average values of these forces are determined for each time step. Fig. 5(a) and 5(b) present plots of average shear and normal forces on the previously printed layer as functions of time. Results from the present work as well as Wang, et al. [34] are plotted. These plots show excellent agreement between the two. There is some noise in the computed data for both cases due to the probabilistic nature of the initial arrangement of particles. However, the magnitudes of the forces are quite similar. As listed in Table 2, the average shear and normal forces from the present work are 0.610 μN and 1.787 μN, compared to 0.639 μN and 1.799 μN from past work, for an error of 4.5% and 0.67%, respectively. One possible reason behind the small disagreement between the two is related to the seed number, which is used to randomly generate the powder particles at the initial time. Although the particle size distribution is the same in both the models,

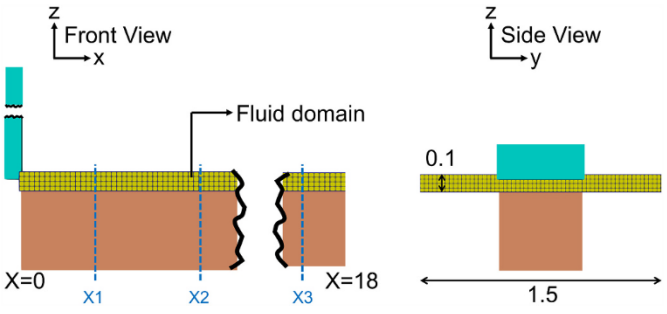

Fig. 4. Schematic showing the position of the 100 μm fluid domain generated on top of the substrate for void fraction characterization.

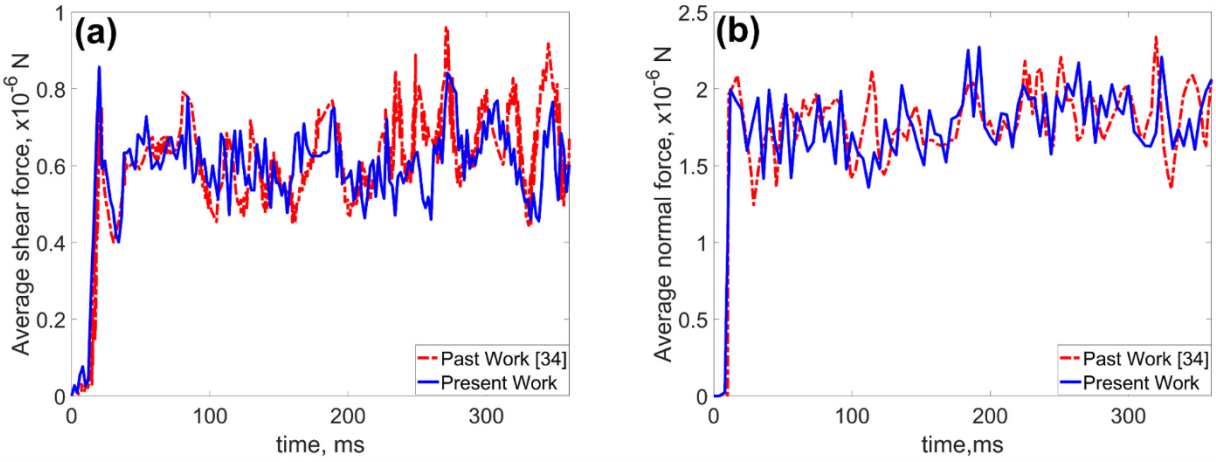

Fig. 5. Comparison of present work with past results [34] for the case of conventional configuration: Average (a) shear and (b) normal forces on the layer underneath as functions of time during the spreading period. Results from present work and past work are both plotted.

Table 2
Comparison between present work and past work [34] in terms of average shear and normal forces exerted on the previously deposited layer between 100 and 300 ms.

	Present Work	Past Work [34]	% Deviation
Average Shear Force (μN)	0.610	0.639	4.5%
Average Normal Force (μN)	1.787	1.799	0.7%

the seed number randomly determines the initial location of the particles within the specified region, which may slightly influence the force computation. Nevertheless, the average shear and normal forces over a certain time, say between 100 and 300 ms, for the present simulation are found to be very close to the values reported by Wang, et al. [34], which is encouraging.

For further validation of the present simulation technique, a comparison of normal force chain contours with Wang, et al. [34] is presented in Fig. 6. Force chains are computed by calculating the contact forces between any pair of granular particles. Once the contact forces are computed, the force chains are visualized in ParaView post-processing software [49]. As shown in Fig. 6, force chain contours from the present work and Wang, et al. [34] are in good agreement with each other in terms of the force magnitude. In both cases, Fig. 6 shows that long force chains occur in the region where the powders are more compact. This region is located in the bottom-left corner of the powder pile in each case, as highlighted by a rectangular box in Fig. 6. This is because as the spreader moves, it compacts the powder particles that are closest to the blade, resulting in the left side of the pile being the most compact. Simultaneously, the self-weight of the powder particles tends to compress the bottom-most layer, resulting in longer force chains with higher force magnitude at the bottom.

Good agreement with Wang, et al. [34] as illustrated in Figs. 5 and 6 provides additional confidence in the powder bed simulation developed in this work.

3.2. Impact of horizontal compactors

The technique of spreading of a loose powder pile followed by densification to the required dimensions of the powder layer based on horizontal compactors (shown in Figs. 1(b) and 2(b)) is studied next through the simulation framework developed here. The magnitude of the force chains, and therefore, the normal and shear force magnitudes can be reduced by dispersing the same number of powder particles over a larger area of the substrate, because this decreases the height of the powder pile. This must be followed by appropriate densification in order to achieve the required powder bed configuration.

To begin with, a set of simulations is carried out to analyze the conventional powder bed configuration with the technique proposed here. Process parameters are assumed to be the same as prior Figures and Table 1. The particle diameter varies from 5 to 65 μm with a normal distribution. The spreader speed is 0.05 m/s, which spreads a powder layer with a thickness of 70 μm. The coefficients of sliding and rolling friction between particles are assumed to be 0.3 and 0.005 respectively [34]. The coefficient of sliding friction between the particles and the substrate is 0.9. Other parameters, such as coefficient of sliding friction between the particles and the wall, coefficient of restitution and coefficient of energy density are also accounted for. The

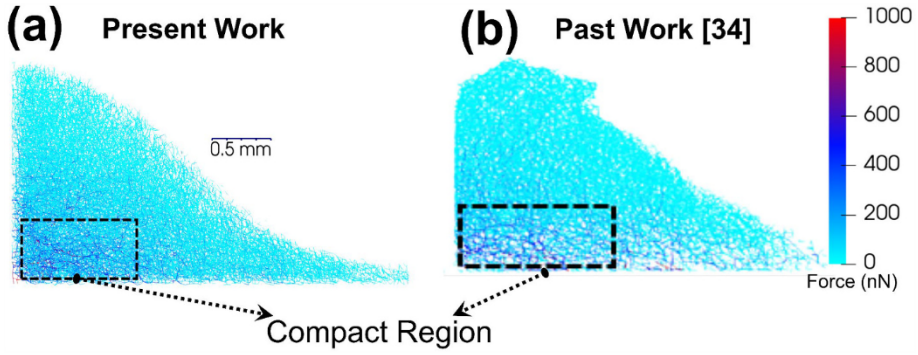

Fig. 6. Comparison of present work with past results [34] for the case of conventional configuration: Contour plots of normal contact force chains showing compact regions in the powder pile.

horizontal compactors are made to move towards each other at a default speed of 0.01 m/s until the particles are compacted, and the powder layer dimensions are the same as the conventional spreading process.

Results for these simulations are presented in Fig. 7 in terms of top view of the powder bed at the end of the process for both cases. Fig. 7 shows a much denser powder layer deposition with the present technique than the conventional configuration case. This is primarily due to the lower inter-particle contact forces caused by the presence of the wall, which improves the spreadability of the powder particles. The final layer height is found to be roughly the same in both cases. Particle segregation can be visualized, which is also consistent with past work [30]. Most of the smaller particles are found near the front and mid sections, while larger particles remain in the back end of the substrate, thus generating a powder layer with varying bulk density along the spreading direction.

For further understanding of the impact of the horizontal compactors, a comparison of force chain contours during the spreading process for the conventional and unconventional configuration cases is shown in Fig. 8. This comparison clearly shows decreased force magnitude due to the implementation of the horizontal compactors. The compact region highlighted by a box in Fig. 8 is of particular interest here, because this is where force chains formed are mainly responsible for force transmission to the previously printed layer, as this region contains force chains of comparatively larger magnitudes. A change in the height of the force chain pile is clearly visible which is due to the increase in the area of the substrate. Further, a comparison of average inter-particle forces as a function of time for both cases is presented in Fig. 9. These data clearly show around 50% reduction in average inter-particle force as a result of the implementation of the horizontal compactors, thereby demonstrating the key benefit of the horizontal compactors. Note that this plot is divided into two phases – the spreading phase, up to 360 ms, and the densification phase, between 360 and 400 ms. Contact forces are lower in the densification phase than in the spreading phase. This is because the powder particles are spread over a larger area during densification, which leads to fewer particle contacts, which lowers the contact forces. An important inference from this plot is that the higher the substrate area, the lower the contact forces. Also, the inter-particle forces begin to decrease after around 320 ms and eventually reach zero, because the particles in the powder pile fall off the substrate.

3.3. Void fraction results

The quality of the powder bed is investigated by calculating its bulk density based on results from CFD-DEM simulations. Fig. 10 shows contours of void fraction for the case of conventional configuration. Small variation in the layer densities along each slice can be visualized from the contour plot shown in the figure. This non-uniformity in layer density along the spreading direction shows the low quality of the powder layer. Fig. 11 plots the void fraction along the *y* direction at sections X1, X2 and X3. Regions in this plot that show a void fraction of close to one have no powder particles, which is clearly undesirable. The large variability in void fraction at each section indicates the poor quality of the powder bed due to particle segregation, as discussed in Section 3.2. The minimum void fraction achieved in this case is around 0.35, which indicates that around 65% of the region is filled with powder particle.

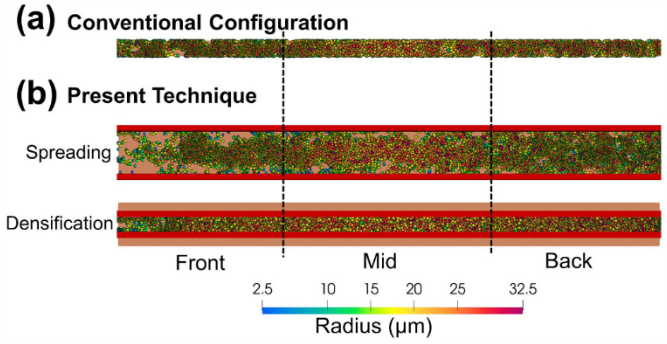

Fig. 7. Top views of powder layer formation showing particle dispersion along the powder layer after spreading and densification for (a) conventional configuration and (b) present technique.

This simulation is repeated for the case with horizontal compactors. The particle properties and size distribution, layer thickness, and spreading speed are all kept constant. Results for this case are shown in Fig. 12. Fig. 12(a) and 12(b) present void fraction contours at each section X1, X2, X3 during loose spreading and densification phases. Compared to conventional configuration case in Fig. 10, the layer density along each section after densification is much more uniform, indicating an improvement in the quality of the powder layer. Void fraction cross section plots shown in Fig. 13(a) and 13(b) indicate that fluctuations in void fraction at each section X1, X2 and X3 are much lower than the baseline conventional configuration case. The minimum void fraction in this case is 0.17, implying that 83% of the region comprises of power particles. This represents around 28% improvement in bulk density due to the use of horizontal compactors.

3.4. Stress analysis on the layer underneath

In addition to the improvement in bed quality as represented by the void fraction discussed in the previous section, stresses acting on the layer beneath the spreading layer are also studied and quantified. It is important to quantify the stress on the previously printed layer because it may cause undesirable geometric distortion of the part. Shear and normal stresses acting on the previously printed layer during the spreading/densification process are computed on the basis of the average shear or normal force over a number of points as follows:

$$\sigma_{shear,ave} = \frac{F_{shear,ave}}{A} = \frac{1}{NA}\sum_{n=1}^{N} F_{shear,n} \tag{1}$$

$$\sigma_{normal,ave} = \frac{F_{normal,ave}}{A} = \frac{1}{NA}\sum_{n=1}^{N} F_{normal,n} \tag{2}$$

where $F_{shear,\ n}$ and $F_{normal,\ n}$ are the shear and normal forces at the n^{th} contact point, and A is the contact area of the powder pile with the substrate at a given instant of time The contact points are obtained from the geometry file. The computed shear and normal stresses are plotted as functions of time in Fig. 14(a) and 14(b), respectively. These plots show significant reduction in both shear and normal stresses during the spreading period due to the horizontal compactors. In the conventional case without the bed wall, the stresses go to zero during the densifying phase as there is no interaction with the bed walls. In the case with bed wall, there is a slight shear stress fluctuation, while the normal stress remains nearly constant. The inter-particle contact forces in the densification phase predominantly contribute towards increasing the sheer stress on the previously printed layer and not the normal stress, which can be observed by comparing Figs. 9 and 14.

The effect of wall speed on the stresses generated on the previously printed layer is analyzed next. Results presented in Fig. 15 show that both shear and normal stresses increase with increasing speed of densification. This is an important trade-off to consider in process design, since high densification speed may be desirable for increasing the printing speed. Fig. 15 also shows that shear stress builds up slowly as the bed walls move inwards. A small magnitude of normal stress is present throughout, due to the weight of powder particles. In contrast, the shear stress at the start of the spreading process is not zero, due to the motion of particles that slide on top of the part before spreading, as the particles are generated and dropped randomly onto the specified region of the substrate using the rain drop method.

Finally, a simulation is carried out to understand the effect of

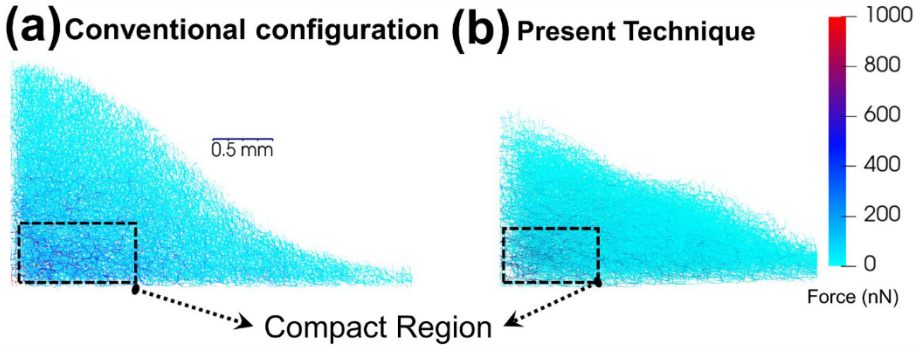

Fig. 8. Contour plots of normal contact force chains within the powder pile for (a) conventional configuration and (b) present technique.

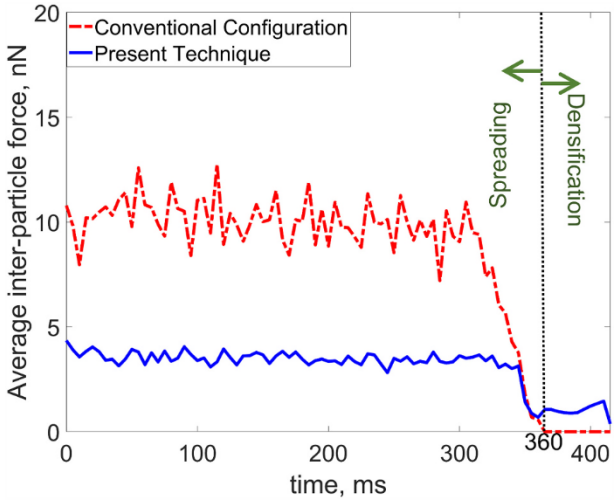

Fig. 9. Average inter-particle force as a function of time during spreading and densification periods, showing comparison between (a) conventional configuration and (b) present technique.

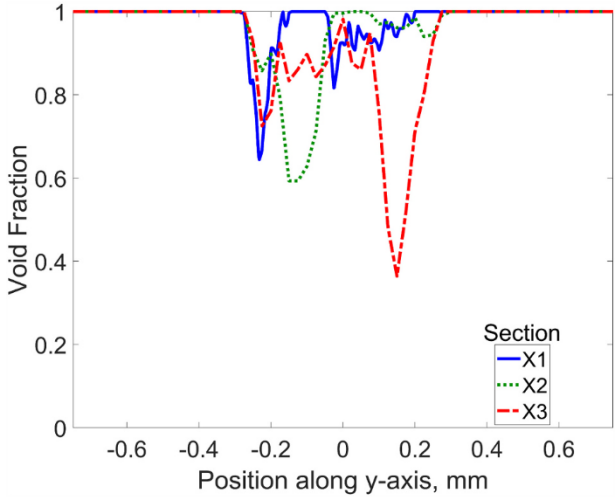

Fig. 11. Plot of void fractions as a function of y at a height of 35 μm from the substrate for the conventional configuration. Data are shown at three different cross-sections shown in Fig. 3.

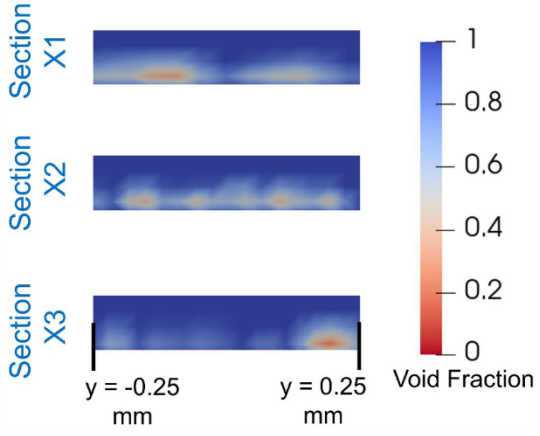

Fig. 10. Contour plot of void fraction at three cross-sections shown in Fig. 3 at the end of the spreading period for the conventional configuration.

increasing the number of particles on the stresses acing on the previously printed layer. Fig. 16 plots normal and tangential stresses as functions of time during both spreading and densification periods, for three different number of powder particles. Fig. 16 shows that the higher the number of particles, the higher are the normal and tangential forces during the spreading period. This is due to greater weight of the powder bed (normal force) and more particles being dragged along the substrate (tangential force). In contrast, normal and shear stresses do not change much with increase in the number of particles during the densifying phase. This is because once the powder is dispersed into a larger area after the spreading process, the area of the powder pile in contact with the substrate also increases, reducing the stresses acting below. The dimensions of the powder pile, especially its area of contact with the substrate determines the amount of stress acting on the layer underneath.

4. Conclusions

Given the critical importance of efficient powder bed packing in ensuring good quality of PBF-printed parts, this work evaluates the use of horizontal compactors to densify the powder layer and reduce forces on the layer underneath. DEM-based simulations are found to be in good agreement with past work. These simulations help understand the distribution of powder particles during spreading and densification. Further, bulk density of the spread powder layer is determined through integration with a grid-based volumetric calculation within a CFD framework. Stresses acting on the layer below in both normal and tangential directions are computed using LIGGGHTS DEM software. It is shown that the use of horizontal compactors results in a higher powder layer quality. Influence of speed of the horizontal compactors and the number of particles on the stress acting on the layer below is also analyzed. It is found that both shear and normal stresses increase with increase in densifying speed and number of particles.

The fundamental concept of horizontal compaction could be

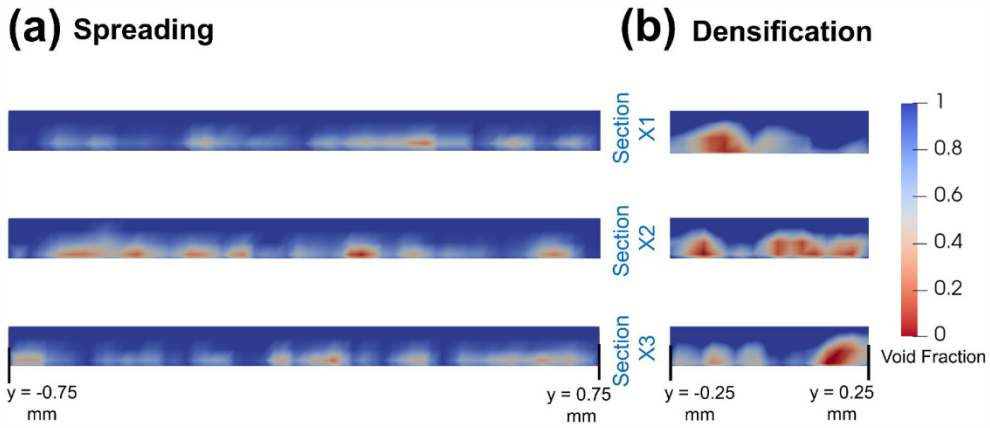

Fig. 12. Contour plot of void fraction at three cross-sections shown in Fig. 3 for the present technique. Plots are presented at the end of (a) spreading period, (b) densification period.

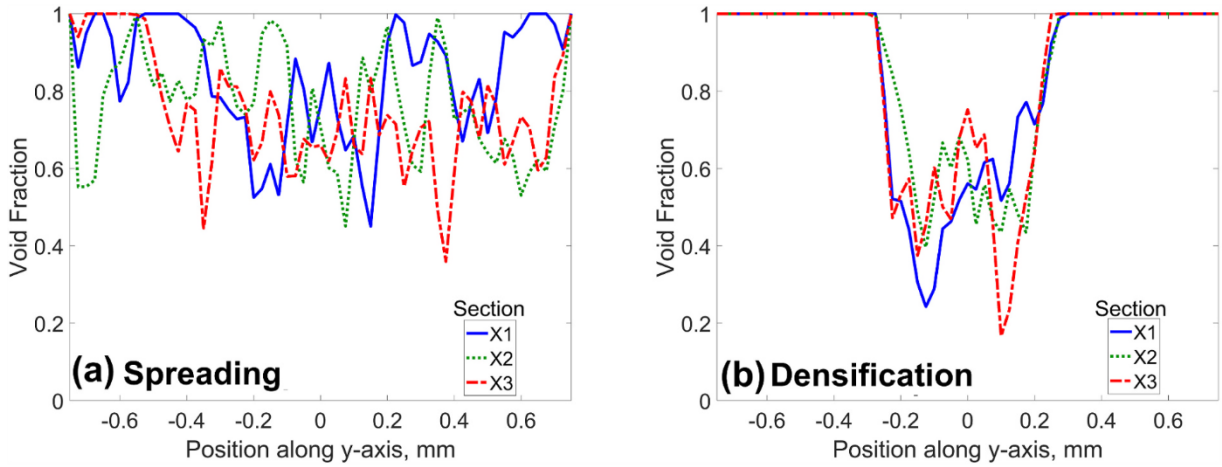

Fig. 13. Plot of void fractions as a function of y at a height of 35 μm from the substrate for the present technique. Data are shown at three different cross-sections shown in Fig. 3. (a) and (b) present data before and after densification.

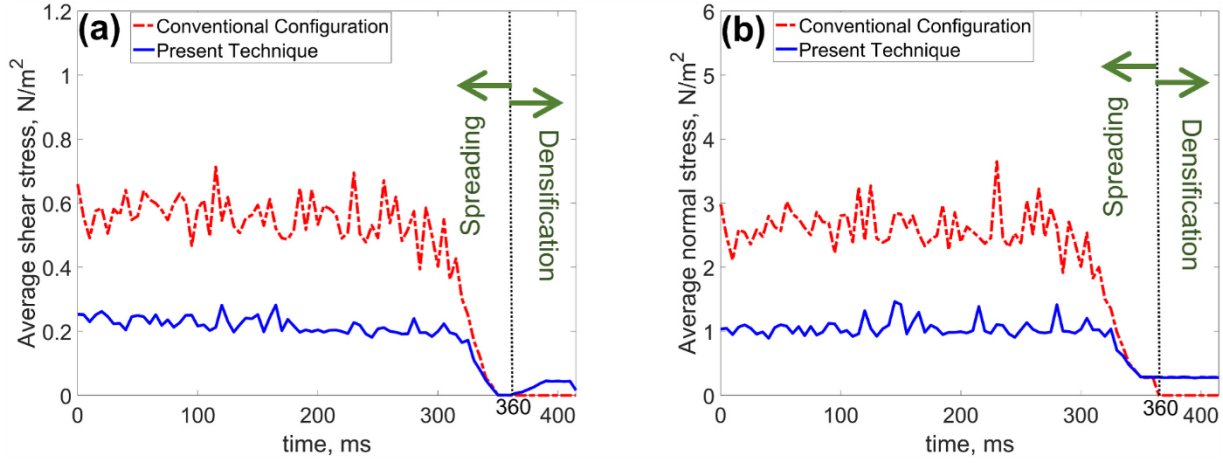

Fig. 14. Plot of average stress during spreading and densification periods without and with bed walls. (a) and (b) plot average shear and normal stress, respectively.

implemented in practical systems in several different ways. One possible implementation is illustrated in Fig. 17 that shows horizontal compaction coupled with downwards bed lowering in order to print multiple layers. A layer of particles is spread (step (a)) and horizontally compacted (step (b)). Then, the layer is sintered and the central region of the bed is lowered (step (c)), thereby making space for the subsequent layer. Compactors are repositioned wide (part (d)), and a new layer of particles is spread (part (e)). Finally, compacting and sintering of the second layer is carried out. These steps are repeated several times in order to print a multi-layer part.

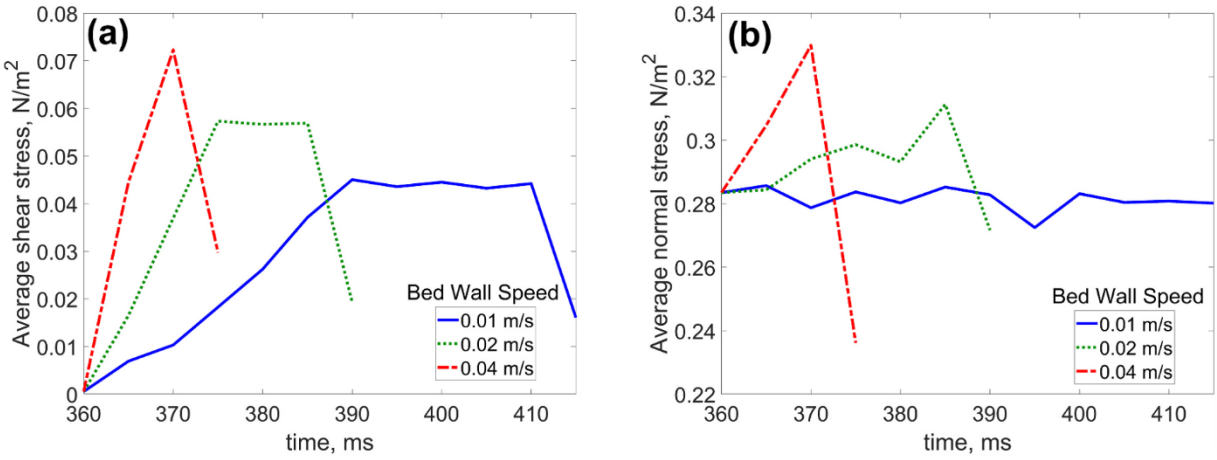

Fig. 15. Plot of average stress during densification period for three different values of densification speed. (a) and (b) plot average shear and normal stress, respectively.

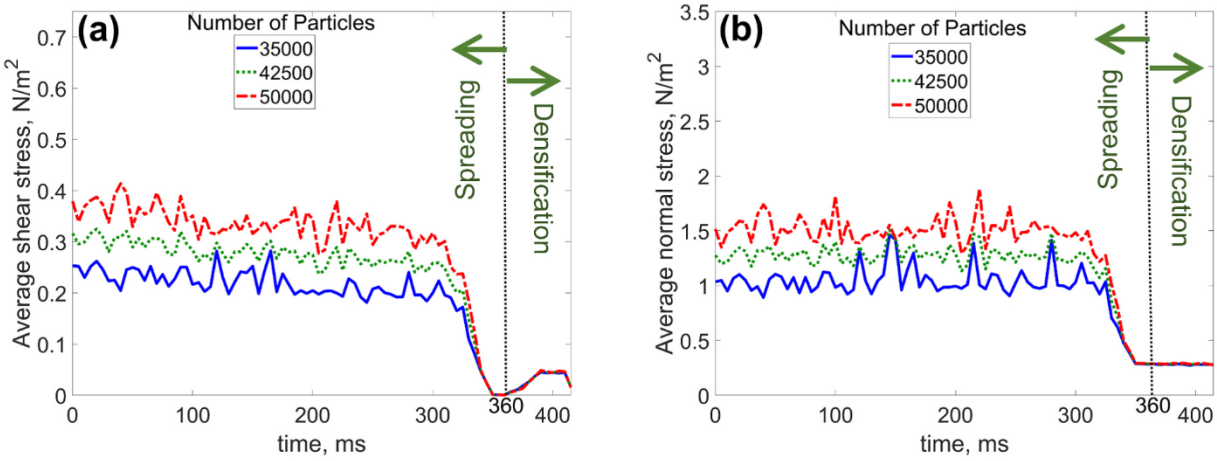

Fig. 16. Plot of average stress during spreading and densification periods for three different values of total number of particles. (a) and (b) plot average shear and normal stress, respectively.

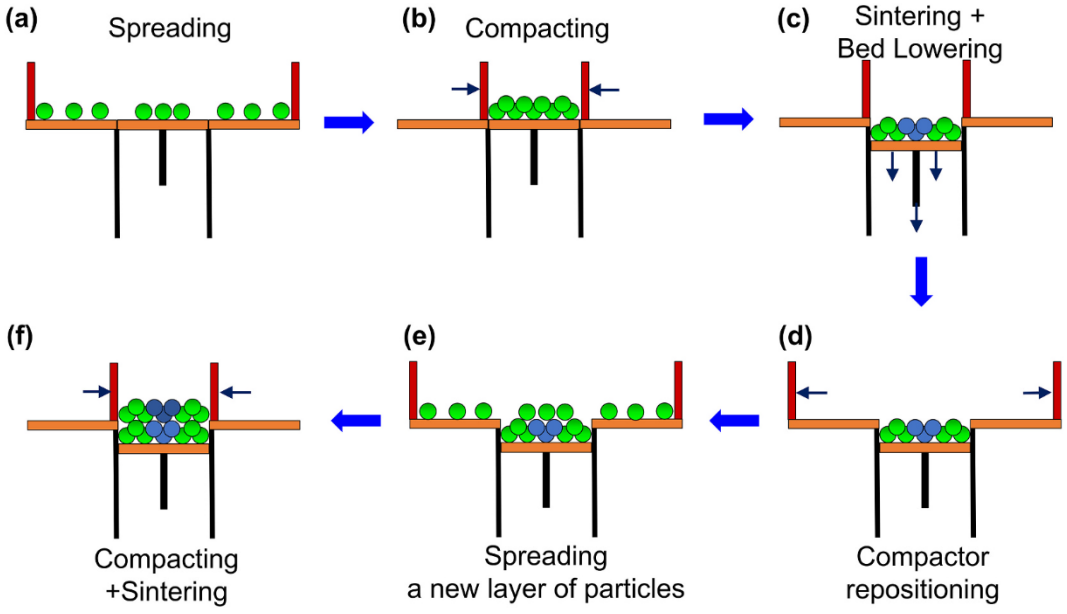

Fig. 17. Illustration of a possible integration of horizontal compacting with downwards lowering of the bed for multi-layer printing.

It is important to note the key assumptions underlying this work. Even though particle-substrate interactions have been modeled through a coefficient of friction, the present work does not account for geometrical irregularities on the substrate, which may be important if the substrate is very rough. Accounting for this effect is expected to result in predictions of a more non-homogeneous powder layer. Other key assumptions in this work include perfectly spherical particles and no vibrations associated with moving parts such as spreader and compactor. Finally, the impact of horizontal compaction on roughness of the formed powder layer has not been studied in this work, and is recommended for future study.

These results help improve the fundamental understanding of powder bed spreading and densification in PBF, and represent a useful tool for design and optimization of practical PBF systems. While studied in the context of laser PBF, the simulation tools developed here may help in the design and analysis of other related additive manufacturing techniques as well.

CRediT authorship contribution statement

Vishnu V. Ganesan: Conceptualization, Methodology, Formal analysis, Validation, Investigation, Data curation, Writing – original draft, Writing – review & editing. **Amirhesam Amerinatanzi:** Validation, Investigation, Writing – original draft, Writing – review & editing. **Ankur Jain:** Conceptualization, Methodology, Validation, Investigation, Project administration, Writing – original draft, Writing – review & editing.

Declaration of Competing Interest

None.

References

[1] K. Wong, A. Hernandez, A review of additive manufacturing, in: International Scholarly Research Notices 10, 2012, p. 208760, https://doi.org/10.5402/2012/208760.

[2] D. Bourell, J. Kruth, M. Leu, G. Levy, D. Rosen, A. Beese, A. Clare, Materials for additive manufacturing, CIRP Ann. 66 (2017) 659–681, https://doi.org/10.1016/j.cirp.2017.05.009.

[3] A. Khorasani, I. Gibson, J.K. Veetil, et al., A review of technological improvements in laser-based powder bed fusion of metal printers, Int. J. Addit. Manuf. Technol. 108 (2020) 191–209, https://doi.org/10.1007/s00170-020-05361-3.

[4] M. Attaran, The rise of 3-D printing: the advantages of additive manufacturing over traditional manufacturing, Business Horizons 60 (2017) 677–688, https://doi.org/10.1016/j.bushor.2017.05.011.

[5] R. Anitha, S. Arunachalam, P. Radhakrishnan, Critical parameters influencing the quality of prototypes in fused deposition modelling, J. Mater. Process. Technol. 118 (2001) 385–388, https://doi.org/10.1016/S0924-0136(01)00980-3.

[6] Y. Kok, X.P. Tan, P. Wang, M.L.S. Nai, N.H. Loh, E. Liu, S.B. Tor, Anisotropy and heterogeneity of microstructure and mechanical properties in metal additive manufacturing: a critical review, Mater. Des. 139 (2018) 565–586, https://doi.org/10.1016/j.matdes.2017.11.021.

[7] H. Prajapati, D. Ravoori, R. Woods, A. Jain, Measurement of anisotropic thermal conductivity and inter-layer thermal contact resistance in polymer Fused Deposition Modeling (FDM), Addit. Manuf. 21 (2018) 84–90, https://doi.org/10.1016/j.addma.2018.02.019.

[8] C.A. Chatham, T.E. Long, C.B. Williams, A review of the process physics and material screening methods for polymer powder bed fusion additive manufacturing, Prog. Polym. Sci. 93 (2019) 68–95, https://doi.org/10.1016/j.progpolymsci.2019.03.003.

[9] G. Nicoletto, R. Kone, M. Frká, E. Riva, Surface roughness and directional fatigue behavior of as-built EBM and DMLS Ti6Al4V, Int. J. Fatigue 116 (2018) 140–148, https://doi.org/10.1016/j.ijfatigue.2018.06.011.

[10] I. Gibson, D. Rosen, B. Stucker, A. Kohsarani, Powder bed fusion, in: Additive Manufacturing Technologies, 2020, pp. 125–170, https://doi.org/10.1007/978-3-030-56127-7_5.

[11] H. Gong, K. Rafi, H. Gu, T. Starr, B. Stucker, Analysis of defect generation in Ti – 6Al – 4V parts made using powder bed fusion additive manufacturing processes, Addit. Manuf. 1–4 (2014) 87–98, https://doi.org/10.1016/j.addma.2014.08.002.

[12] A. Averardi, C. Cola, S.E. Zeltmann, N. Gupta, E Ff Ect of particle size distribution on the packing of powder beds : a critical discussion relevant to additive manufacturing, Mater Today Commun 24 (2020) 100964, https://doi.org/10.1016/j.mtcomm.2020.100964.

[13] M.A. Balbaa, A. Ghasemi, E. Fereiduni, M.A. Elbestawi, S.D. Jadhav, J. Kruth, Role of powder particle size on laser powder bed fusion processability of AlSi10mg alloy, Addit. Manuf. 37 (2021), 101630, https://doi.org/10.1016/j.addma.2020.101630.

[14] X. Wang, C. Zhu, H. Xie, H. Li, F. Liu, W. Ren, F. Tan, A high-efficiency forming method of large- scale aluminum alloy components using fused deposition additive manufacturing based on multi-energy fields, J. Manuf. Process. 62 (2021) 704–710, https://doi.org/10.1016/j.jmapro.2020.12.065.

[15] J. Lee, Novel fabrication of Alloy 625 and MCrAlY bond coat by laser powder bed fusion and microstructure control, in: Materials. Ecole des Mines d'Albi-Carmaux, Changwon National University, 2020.

[16] W.L. Smith, Effects of Surface Layer Heating on Laser Powder Bed Fusion of 316L Stainless Steel, M.S. Thesis, University of California Davis, 2021.

[17] W. Tucho, V. Hansen, Studies of post-fabrication heat treatment of L-PBF-Inconel 718: effects of hold time on microstructure, annealing twins, and hardness, Metals 11 (2021) 266, 1-19, https://doi.org/10.3390/met11020266.

[18] H.R. Javidrad, S. Salemi, Effect of the volume energy density and heat treatment on the defect, microstructure, and hardness of L-PBF Inconel 625, Metall. Mater. Trans. A 51 (2020) 5880–5891, https://doi.org/10.1007/s11661-020-05992-x.

[19] M. Masoomi, J.W. Pegues, S.M. Thompson, N. Shamsaei, A numerical and experimental investigation of convective heat transfer during laser-powder bed fusion, Addit. Manuf. 22 (2018) 729–745, https://doi.org/10.1016/j.addma.2018.06.021.

[20] W. Yan, S. Lin, O.L. Kafka, et al., Modeling process-structure-property relationships for additive manufacturing, Front. Mech. Eng. 13 (2018) 482–492, https://doi.org/10.1007/s11465-018-0505-y.

[21] H. Chen, Y. Sun, W. Yuan, S. Pang, W. Yan, Y. Shi, A review on discrete element method simulation in laser powder bed fusion additive manufacturing, Chinese J. Mech. Eng. Addit. Manuf. Front. (2022), https://doi.org/10.1016/j.cjmeam.2022.100017 in press.

[22] Y. Lee, S. Simunovic, A. Gurnon, Quantification of powder spreading process for metal additive manufacturing, in: Technical Report ORNL/TM-2019/1380, Oak Ridge National Laboratories, 2019, https://doi.org/10.2172/1615799.

[23] Y.M. Fouda, A.E. Bayly, A DEM study of powder spreading in additive layer manufacturing, Granul. Matter 22 (2020) 10, https://doi.org/10.1007/s10035-019-0971-x.

[24] S. Yim, H. Bian, K. Aoyagi, K. Yamanaka, A. Chiba, Spreading behavior of Ti48Al2Cr2Nb powders in powder bed fusion additive manufacturing process: experimental and discrete element method study, Addit. Manuf. 49 (2022), https://doi.org/10.1016/j.addma.2021.102489.

[25] V. Lampitella, M. Trofa, A. Astarita, G. D'Avino, Discrete element method analysis of the spreading mechanism and its influence on powder bed characteristics in additive manufacturing, Micromachines 12 (2021) 392, https://doi.org/10.3390/mi12040392.

[26] Y. Lee, A.K. Gurnon, D. Bodner, et al., Effect of particle spreading dynamics on powder bed quality in metal additive manufacturing, Integr. Mater. Manuf. Innov. 9 (2022) 410–422, b2020, https://doi.org/10.1007/s40192-020-00193-1.

[27] S. Haeri, Enhancement of the spreading process in additive manufacturing through the spreader optimisation, in: Proc. 5th Int. Conf. on Particle-Based Methods : Fundamentals and Applications, 2017, pp. 409–419.

[28] Y. Zhao, Y. Koizumi, K. Aoyagi, K. Yamanaka, ScienceDirect characterization of powder bed generation in electron beam additive manufacturing by discrete element method (DEM), Mater. Today Proc. 4 (11) (2017) 11437–11440, https://doi.org/10.1016/j.matpr.2017.09.023.

[29] H. Irrinki, M. Dexter, B. Barmore, et al., Effects of powder attributes and laser powder bed fusion (L-PBF) process conditions on the densification and mechanical properties of 17-4 PH stainless steel, JOM 68 (2016) 860–868, https://doi.org/10.1007/s11837-015-1770-4.

[30] U. Ali, Y. Mahmoodkhani, S.I. Shahabad, R. Esmaeilizadeh, F. Liravi, E. Sheydaeian, K.Y. Huang, E. Marzbanrad, M. Vlasea, E. Toyserkani, On the measurement of relative powder-bed compaction density in powder-bed additive manufacturing processes, Mater. Des. 155 (2018) 495–501, https://doi.org/10.1016/j.matdes.2018.06.030.

[31] K. Marchais, J. Girardot, C. Metton, et al., A 3D DEM simulation to study the influence of material and process parameters on spreading of metallic powder in additive manufacturing, Comp. Part. Mech. 8 (2021) 943–953, https://doi.org/10.1007/s40571-020-00380-z.

[32] P. Desai, C.F. Higgs III, A DEM model to predict and correct spreader shear-induced part deformation in binder jet additive manufacturing, in: 14th WCCM-ECCOMAS Congress 2020 vol. 1000, 2021, March.

[33] A.L. Maximenko, I.D. Olumor, A.P. Maidaniuk, E.A. Olevsky, Modeling of effect of powder spreading on green body dimensional accuracy in additive manufacturing by binder jetting, Powder Technol. 385 (2021) 60–68, https://doi.org/10.1016/j.powtec.2021.02.070.

[34] L. Wang, A. Yu, E. Li, H. Shen, Z. Zhou, Effects of spreader geometry on powder spreading process in powder bed additive manufacturing, Powder Technol. 384 (2021) 211–222, https://doi.org/10.1016/j.powtec.2021.02.022.

[35] Eric J.R. Parteli, Thorsten Pöschel, Particle-based simulation of powder application in additive manufacturing, Powder Technol. 288 (2016) 96–102, https://doi.org/10.1016/j.powtec.2015.10.035.

[36] W. Lee, Y. Zhang, J. Zhang, Discrete Element Modeling of powder flow and laser heating in direct metal laser sintering process laser heating holding, Powder Technol. 315 (2017) 300–308, https://doi.org/10.1016/j.powtec.2017.04.002.

[37] M. Khorasani, A. Ghasemi, M. Leary, W.O. Neil, I. Gibson, L. Cordova, B. Rolfe, Numerical and analytical investigation on meltpool temperature of laser-based powder bed fusion of IN718, Int. J. Heat Mass Transf. 177 (2021), 121477, https://doi.org/10.1016/j.ijheatmasstransfer.2021.121477.

[38] J. Zielinski, S. Vervoort, H.W. Mindt, et al., Influence of powder bed characteristics on material quality in additive manufacturing, BHM Berg- und Hüttenmännische Monatshefte 162 (2017) 192–198, https://doi.org/10.1007/s00501-017-0592-9.
[39] D.S. Bassett, D.S. Bassett, E.T. Owens, M.A. Porter, M. Lisa, Extraction of force-chain network architecture in granular materials using community detection, Soft Matter 11 (2015) 2731–2744, https://doi.org/10.1039/C4SM01821D.
[40] H.A. Makse, D.L. Johnson, L.M. Schwartz, Packing of compressible granular materials, Phys. Rev. Lett. 84 (2000) 1–4, https://doi.org/10.1103/PhysRevLett.84.4160.
[41] Y. He, T.J. Evans, A.B. Yu, R.Y. Yang, A GPU-based DEM for modelling large scale powder compaction with wide size distributions, Powder Technol. 333 (2018) 219–228, https://doi.org/10.1016/j.powtec.2018.04.034.
[42] C. Kloss, C. Goniva, et al., Models, algorithms and validation for opensource DEM and CFD–DEM, Prog. Comput. Fluid Dyn. 12 (2012) 2–3, https://doi.org/10.1504/PCFD.2012.047457.
[43] J.F. Peters, M. Muthuswamy, J. Wibowo, A. Tordesillas, Characterization of force chains in granular material, Phys. Rev. 72 (2005) 1–8, https://doi.org/10.1103/PhysRevE.72.041307.
[44] Johnson Kenneth Langstreth, Kendall Kevin, A.D. Roberts, Surface energy and the contact of elastic solids, Proc. R. Soc 324 (1971), https://doi.org/10.1098/rspa.1971.0141.
[45] S. Haeri, Optimisation of blade type spreaders for powder bed preparation in additive manufacturing using DEM simulations, Powder Technol. 321 (2017) 94–104, https://doi.org/10.1016/j.powtec.2017.08.011.
[46] H. Kalman, D. Portnikov, Analyzing bulk density and void fraction : a . the effect of Archimedes number, Powder Technol. 381 (2021) 477–487, https://doi.org/10.1016/j.powtec.2020.12.014.
[47] H.G. Weller, G. Tabor, H. Jasak, C. Fureby, A tensorial approach to computational continuum mechanics using object-oriented techniques, Comput. Phys. 12 (1998) 620, https://doi.org/10.1063/1.168744.
[48] C. Goniva, C. Kloss, N.G. Deen, J.A.M. Kuipers, S. Pirker, Influence of rolling friction modelling on single spout fluidized bed simulations, Particuology 10 (2012) 582–591, https://doi.org/10.1016/j.partic.2012.05.002.
[49] J. Ahrens, B. Geveci, C. Law, J. Ahrens, B. Geveci, C. Law, ParaView : An End-User Tool for Large Data Visualization, Technical Report LA-UR-03-1560, Los Alamos National Laboratory, 1996, https://datascience.dsscale.org/wp-content/uploads/2016/06/ParaView.pdf. accessed 03/11/2022.